AIAA-2004-2802
3-element airfoil

Characterization of Unsteady Flow Structures Near Leading-Edge Slat: Part II. 2D Computations

Mehdi R. Khorrami*, Meelan M. Choudhari*, and Luther N. Jenkins**
NASA Langley Research Center, Hampton, VA, 23681-2199

In our previous computational studies of a generic high-lift configuration, quasi-laminar (as opposed to fully turbulent) treatment of the slat cove region proved to be an effective approach for capturing the unsteady dynamics of the cove flow field. Combined with acoustic propagation via Ffowcs Williams and Hawkings formulation, the quasi-laminar simulations captured some important features of the slat cove noise measured with microphone array techniques. However, a direct assessment of the computed cove flow field was not feasible due to the unavailability of off-surface flow measurements. To remedy this shortcoming, we have undertaken a combined experimental and computational study aimed at characterizing the flow structures and fluid mechanical processes within the slat cove region. Part I of this paper outlines the experimental aspects of this investigation focused on the 30P30N high-lift configuration; the present paper describes the accompanying computational results including a comparison between computation and experiment at various angles of attack. Even though predictions of the time-averaged flow field agree well with the measured data, the study indicates the need for further refinement of the zonal turbulence approach in order to capture the full dynamics of the cove's fluctuating flow field.

I. Introduction

With the projected growth in air travel, population centers adjacent to airports will be subjected to higher noise levels due to the increased number of landing and departing aircraft. A high priority goal of NASA is to diminish the environmental noise impact of air travel. NASA's stated goal is to reduce aircraft noise by a factor of four by year 2022, relative to 1997 best-in-fleet technology. Obviously, mitigation of the airframe (nonpropulsive) component of aircraft noise is integral to this ambitious goal.

Future design of airframes that have minimal noise signatures requires the development of a new breed of engineering noise analysis tools with improved predictive capabilities. Certainly, for these engineering models to become a reality, a fundamental knowledge of airframe noise sources and the underlying noise generation mechanisms is a prerequisite. To acquire such basic knowledge, one must start with a synergistic computational and experimental effort that would allow attention to be focused on a particular noise source of interest. In this paper, we present our recent computations of a leading-edge slat with the primary focus on the unsteady fluid dynamics of the cove region. The companion experimental results, used for validating the current simulations, are reported in Jenkins, Khorrami, and Choudhari.[1]

Model scale tests[2-6] and flyover noise measurements[7] have established the leading-edge slat as a prominent source of airframe noise during aircraft approach and landing. These tests have revealed that the slat by itself is a complex aeroacoustic problem composed of several competing noise generation mechanisms. Detailed acoustic measurements obtained by Dobrzynski et al.[6] and at NASA[2-3] showed that the slat acoustic spectrum contains both broadband and high-frequency tonal components. The high-frequency tonal sound was shown to be associated with

*Aerospace Technologist, Computational Modeling and Simulation Branch, Associate Fellow AIAA
**Aerospace Technologist, Flow Physics and Control Branch

the slat trailing edge, and its noise generation mechanism (vortex shedding from a finite thickness edge) is now well understood.[8-9] While early noise reduction studies[3,6] attributed the broadband noise component to the slat cove flow field, the precise noise generation mechanisms remained elusive. In an effort to relate the far field acoustics to the noise-producing flow structures in the near field, a series of numerical studies[10-12] were undertaken at NASA Langley Research Center (LaRC). The two-dimensional (2D) simulations were aimed at simulating the aeroacoustic tests of the Energy Efficient Transport (EET) high-lift model in the Low Turbulence Pressure Tunnel (LTPT) at NASA LaRC. The computational framework of unsteady Reynolds-averaged Navier-Stokes (URANS) equations coupled with the Ffowcs Williams and Hawkings (FWH) formulation of acoustic analogy was used to calculate the far field acoustics. These computations further reinforced the connection between cove flow unsteadiness and the radiated broadband noise. A comprehensive list of references and a summary of NASA LaRC efforts, focused on slat noise, is provided in Khorrami et al.[13] and Khorrami.[14] Only the pertinent results are reiterated here.

The initial fully turbulent simulations of Khorrami et al.[10] were found to be deficient. They proved to be overly diffusive and thus prevented the proper development of cove flow unsteadiness. To circumvent the excessive diffusive effects of the turbulence model, a simple zonal approach based on physical arguments was advocated and pursued by Khorrami, Singer, and Lockard[11] and Choudhari, Khorrami, Lockard, Atkins, and Lilley[12] (hereafter referred to as KSL and CKLAL, respectively). These authors argued that the energy-containing, large-scale coherent structures in the cove region are predominantly responsible for the far field noise. As a practical (but ad hoc) approach to understanding the associated noise generation processes, they began by resolving only 2D large-scale structures,[11, 12] and the turbulence production due to unresolved scales of motion was zeroed out within a limited zone enclosing the cove area. The zonal, quasi-laminar unsteady simulations produced far field acoustic spectra that agreed in shape (but not in levels) with the LTPT microphone array measurements. In addition, observed trends such as angle of attack (AOA) effects on slat noise as well as velocity scaling laws and high-frequency roll-off in the slat noise spectrum were all duplicated in a reasonable manner. The simulated cove flow fields displayed complex and highly nonlinear flow dynamics. Important stages within the cove recirculation zone, such as shear layer oscillation and roll-up, formation of large-scale coherent structures, vortex merging, and the ejection of vortices through the slat gap, were captured.

Statistical analysis of the computed unsteady flow field by CKLAL confirmed the presence of increased fluctuation levels within the shear layer emanating from the slat cusp, as well as revealing additional hot spots in the turbulent kinetic energy (TKE) distribution near the reattachment point, in the vicinity of the slat cusp, and (at low angles of attack) in the central zone of the cove recirculating flow. Although intensified turbulent flow activity was expected in the shear layer and near the reattachment point, the elevated TKE levels in the recirculating flow near the cusp and within the cove center had not been predicted by steady-state calculations based on a conventional, two-equation turbulence model. The increased TKE levels in regions adjacent to the slat bottom surface and the cove center are due to the longevity of vortices entrapped in the cove region, their interaction with the slat undersurface, and the emergence of a large and strong vortex in the center of the recirculating zone. Certainly, it may be argued that the energetic nature of the trapped vortices and their lingering effects were partly the result of the reduced turbulent diffusion encountered within the quasi-laminar cove. The difficult question to answer is, to what degree? Of course, a direct comparison of the predicted cove flow field with experimental measurements would have helped settle this issue. Unfortunately, a lack of suitable near field measurements for the EET model prevented a direct validation of the computed near field solutions. Based on CKLAL's partial comparison of the computed turbulent statistics and measurements of Takeda et al.,[15] the validity of both the intense near-wall turbulent fluctuations (associated with vortex-induced separation of the recirculating flow) and the presence of the strong cove center vortex were raised as unresolved issues. However, the above comparison was somewhat limited by the measurements and the differences in high-lift configurations involved. In particular, the Laser Doppler Velocimeter (LDV) measurements of Takeda et al. were performed for a different high-lift geometry than our EET model. The model settings (e.g., slat and flap deflection angles, AOA, gaps, etc.) in the European test were also different than the in-house LTPT experiments modeled in the computations. Finally, the measurements lacked sufficiently detailed resolution of the slat cusp region, where considerable activity was detected in the computations of KSL and CKLAL. We note in passing that effects of three-dimensional (3D) flow structures neglected in the above computations were included in recently reported large-eddy simulations of Terracol et al.;[16] however, again, a direct validation of the near field predictions was not possible due to the lack of experimental data for their high-lift configuration. A brief summary of previous experiments pertaining to slat cove flow is provided in Part I of this paper.[1]

The present paper continues our effort towards gaining a fundamental understanding of noise generation mechanisms associated with a leading-edge slat in a high-lift configuration. Following the framework established by KSL and CKLAL, the current effort attempts to shed additional light on the unresolved questions involving the development of unsteady flow structures, the nature of interaction between these structures and slat solid surfaces, and the evolution of the recirculation zone. At this point, our goal is to evaluate the accuracy of the zonal model employed previously and attempt to resolve some of the major issues raised by previous studies before extending the present approach to include 3D effects.

II. High-Lift Model Geometry

As stated in the introduction, our previous efforts were focused on simulating the EET high-lift configuration that was tested in the LTPT facility at NASA LaRC. For our current effort, we decided early on to perform the validation tests in the Basic Aerodynamic Research Tunnel (BART) at LaRC. The advantages of switching to BART were twofold. First, because of its better optical access and overall ease of access to the test section, it is a more suitable facility to conduct detailed off-surface fluid dynamics measurements. Second, BART provides a more cost-effective environment than the pressurized LTPT facility. We note that, due to the relatively close proximity of tunnel walls to the model, acoustic measurements in BART may not provide meaningful information concerning the far field acoustics; however, that was not deemed to be a major handicap in view of our focus on near field flow measurements.

For the current validation tests, rather than modifying the EET model to fit BART's narrower test section, we switched to an alternate high-lift model that had already been tested in this facility. The current model, known as the 30P30N model in the open literature, is a three-element, high-lift configuration composed of a slat, main element, and flap. The numerals contained in the model name represent slat and flap deflection angles (30 degrees each), respectively. The 30P30N, designed by McDonnell-Douglas (now Boeing), predates the EET model. Although there are differences, the sectional profile of the 30P30N model (shown in Fig.1) is similar to the EET profile.

The stowed chord of the 30P30N model tested in BART is 0.457 m (18 inches) compared to the EET's 0.55 m chord. The slat chord and flap chord are 15% and 30% of the stowed chord, respectively. The Reynolds number based on the stowed chord equals 1.7 million at the test speed of M = 0.17. This Reynolds number is somewhat lower than the range beyond which Reynolds number effects were found to become negligible during the EET experiments;[3] however, the subsequent comparison with computations demonstrates that the Reynolds number of the model we used was adequately large for the purpose of this investigation. The rigging parameters for the 30P30N high-lift configuration are listed in Table I. As tested, all three elements had blunt trailing edges. For present simulations, the trailing edges of the main element and the flap were artificially sharpened while preserving the respective values of camber. The trailing edge of the slat is 0.36 mm (0.014 inches) thick and was well resolved in the computations.

Table I. Geometrical Settings

Slat angle, δ_s	30°
Flap angle, δ_f	30°
Slat Gap, g_s	2.95%
Flap Gap, g_f	1.27%
Slat Overhang, o_s	-2.5%
Flap Overhang, o_f	0.25%

III. Grid Topology

The similarity of the cross-sectional profiles allowed us to easily adapt the EET grid to the current geometry. Additional refinements were introduced in key areas such as the slat cove and main element underside. Patched (i.e., nonconforming) zone interfaces were used as necessary to prevent the propagation of fine grids to unwanted regions.

The present 2D mesh is composed of 22 blocks containing a total of 698k nodes. Out of this total, 171k points reside within the block covering the slat cove region. As a comparison, the corresponding numbers for the EET grid are 427k and 99k points, respectively. To allow direct comparison with the measurements, the entire length of the tunnel test section was simulated during the computations, with the top and bottom tunnel walls treated as inviscid boundaries. Because of the close proximity of the tunnel walls (0.8 chords) to the test model, a significant number of grid points were clustered between the model underside and the tunnel floor to capture, as much as possible, reflected acoustic waves from the solid walls (Fig.2).

IV. Numerical Approach

A. Flow Solver

Similar to our previous studies,[8,10-12] the CFL3D code developed at NASA LaRC was employed to compute the flow field. The time-accurate computations were performed by using the second-order time discretization and the "dual time stepping" technique. Twenty subiterations, in conjunction with three-level V-type multigrid cycles, were used to obtain several orders of magnitude drop in both global and turbulence model residuals during each time step.

B. Turbulence Model

The two-equation Shear Stress Transport (k-ω) model of Menter[17] is selected to be the preferred model for the present problem. As a starting point, we followed the zonal turbulence approach of KSL in order to validate the effectiveness of this methodology in capturing the full dynamics of the cove flow field. That is, in accordance with the KSL study, the turbulent production term in the turbulence transport equations was switched off within the slat cove region to eliminate the excessive diffusive effects of the turbulence model.

V. Results and Discussions

Unless indicated otherwise, normalized results presented in this paper are scaled with respect to the stowed chord and free-stream velocity, density, and molecular viscosity. To match the experimental conditions, the 2D simulations are carried out for M = 0.17 and Re = 1.71×10^6. Given the nearly equivalent sizes of EET and 30P30N models, KSL's nondimensional time step of $\Delta t = 4.116 \times 10^{-4}$ (scaled by free-stream acoustic speed and the stowed chord), which is equivalent to a resolution of 200 time steps per period for a 7.5 kHz signal, is retained in the present computations. To capture the effects of AOA variation on the local flow dynamics, URANS computations for angles of 8, 6, and 4 degrees were performed. The selected angles cover the typical approach conditions that are of prime interest here.

All of the present simulations were run in a steady, fully turbulent mode first, until the variation in the global lift and drag coefficients became less than 0.5% of the mean values. This procedure helped eliminate the strong cove center vortex, which was identified in CKLAL as a questionable feature of the earlier computations. Because of the fine resolution of the slat cove region, even in the steady mode, the detached shear layer showed signs of low-amplitude undulations that resulted in a weak and slow roll-up of the shear layer. Nevertheless, as will be shown later, the steady solutions do provide the correct surfaces pressures. When it comes to off-surface mean quantities however, the stationary flow field must be extracted by time averaging the unsteady solutions.

The time-accurate simulations were carried out with the quasi-steady solutions described above as the starting point. For each simulation, to minimize the effects of the initial transient state on both mean flow and statistical quantities, the solution during the first 6000–7000 time steps was discarded. (For reference, it requires approximately 2140 time steps for the free-stream flow to convect over a distance equal to the slat chord.) Typically, a record length of 10,000 time steps was used to perform the averaging and to extract the turbulent statistics. Although longer time records are preferable, no significant deviations in mean velocity distribution were noted when the record length was extended to 13,000 time steps in one particular case.

A. Surface Pressure Comparison with Measured Data

For validation purposes, it is useful to begin with a comparison of mean pressure distribution along the surface of each element of the high-lift system. The mean loading determines the acceleration or deceleration of the flow along the surface, which, in turn, has a significant influence on the development of the large-scale unsteady structures. The steady fully turbulent solutions were used to obtain the pressure coefficient, Cp, distributions

presented below. These values were virtually identical to those based on the time average of the unsteady solutions. Figure 3 shows the *Cp* distribution on all three elements at 4-degree AOA. Note that the maximum value of the ordinate has been varied according to the peak suction along each element. Overall, good agreement is observed between the computational fluid dynamics (CFD) solutions and measured data. Both datasets indicate flow separation along the flap surface that extends over 40% of the flap chord. The accuracy of *Cp* predictions near the leading edge of the main element provides some confidence that the slat gap flow field is properly captured. Clearly, the slat is the most critical element for our study; even though it is sparsely populated with pressure taps during the experiment, we can deduce that important trends in *Cp* distribution are captured in the computations. A notable difference from the measured slat pressures involves higher suction values aft of the leading edge along the top surface. As seen in figures 4 and 5, this overprediction of slat suction becomes more pronounced as the AOA increases to 8 degrees. Based on measurements of the spanwise *Cp* distribution (not shown here), this trend was attributed to the strictly 2D nature of our computations that ignores the effects of finite span and tunnel side-wall interference on the measured data.

Figure 4 displays the *Cp* distributions for a 6-degree AOA. At this angle, computed flap separation is larger in extent than that indicated by the measurement, resulting in a noticeable underprediction of the *Cp* along the flap suction surface. This discrepancy may be the result of one or more of the following three factors associated with the computations. First, the chordwise adverse pressure gradient along the flap is somewhat increased by the sharpening of the trailing edge in the computational geometry. Second, the measurement includes the effect of spanwise relief that is absent from the 2D computations. Third, conventional turbulence models are known to have limitations in handling pressure driven flow separation. Once again, however, there is satisfactory agreement between the computed and measured pressures along the main element and the slat for the 6-degree AOA case.

Figure 5 presents the *Cp* distributions at an 8-degree AOA. At this angle, the flap surface pressures indicate a fully attached flow; thus, predicted and measured values of *Cp* along the flap are in full agreement. At the same time, suction side pressures on the main element and slat show increased deviation from the measurement, possibly due to higher finite-span effects at a larger AOA.

B. Off-Surface Time-Averaged Quantities

The off-surface mean quantities were constructed from the time-accurate simulations by averaging over nearly 10,000 time steps. The corresponding PIV results were obtained by averaging over at least 400 snapshots. Figures 6 through 8 show the contours of streamwise (u) and vertical (v) velocity components based on both measurements and computations for the three AOA values examined herein. Overall, good qualitative and quantitative agreement is observed between predictions and the measurements. The increased streamwise velocities near the cusp, evident from the dark red contours in part (a) of Figs. 6 through 8, are accurately predicted by the computations. The magnitude of flow acceleration ahead of the cusp determines the strength of the cove shear layer, a critical parameter in determining the evolution of the unsteady flow structures. Notice that the strength of flow acceleration weakens with an increasing AOA, indicating reduced shear layer strength at higher AOA. This reduction in strength correlates well with the observed trend of reduced slat-noise levels as the AOA is increased. As expected, the highest negative cove velocities, imposed by the recirculating flow field, occur adjacent to the slat wall. Compared with the PIV results, the predicted velocity magnitudes in the cove are slightly higher. The overprediction of velocity magnitudes is believed to be a side effect of the 2D nature of the simulations. Irrespective of AOA, the most notable difference between the measured and predicted velocities occurs near the cusp, where computed u contours show significant penetration of flows with positive velocities towards the cove wall. The penetration is instigated by the gathering and interaction of shear layer vortices that eventually end up inside the recirculating zone and get trapped between the solid wall and the shear layer at the cusp. Lastly, the computed vertical velocity contours show the proper flow acceleration around the main element leading edge and further into the slat gap.

The mean vorticity fields are presented in Fig. 9. Neither measured nor computed fields show evidence of a cove center vortex. Both fields indicate weakening of the shear layer at 8-degree AOA is increased, reinforcing the trend deduced from the mean velocity field. In addition, the PIV results depict a well-defined free shear layer with the vorticity confined to a narrow spatial band. The nearly uniform thickness of the vorticity layer and subsequent lack of spreading suggest that amplification of shear layer disturbances, the roll-up process, and the formation of large-scale coherent structures all occur within a short distance from the cusp where the incoming boundary layer detaches from the wall. In contrast, the computed time-averaged vorticity fields are diffused over a much wider spatial band. Notice the presence of a ring of positive sign vorticity inside the recirculating zone. As described by KSL for the EET configuration at 8-degree AOA, vortices ingested by the recirculating zone travel within a ring that

borders the slat bottom surface and the shear layer interior side, leaving the zone's center devoid of any significant levels of vorticity.

The thick region of negative sign vorticity approaching the cusp is the manifestation of secondary and even tertiary separations, caused by the passage of the ingested vortices over the solid wall. Absent from the measured fields is any sign of such a strong secondary separation. Because the presence of the secondary separation zone affects so many other aspects of the cove flow field, it highlights a major shortcoming of the current simulations. In our view, the existence of such a region (which is not corroborated by the measurements) can be attributed to two distinct factors. The first factor involves the extra viscous effects imposed by the fine scales of a fluctuating field, which have been switched off in our zonal approach. This extra diffusion may enforce the proper decay of the trapped vortices; thus, it plays a prominent role in determining the near-wall flow dynamics. To test this conjecture, we ran additional simulations wherein the turbulence production term was restored in the near wall portion of the cove region. The results showed mixed success. The unsteady eruptions of the recirculating boundary layer were considerably weakened and the mean shear layer was better defined similar to the PIV data; however, a quasi-steady separation that isolated the cusp region from the rest of the circulation zone was found to occur as a result of the modification to the baseline zonal model. The second factor underlying the strong secondary separation is related to the effects of three-dimensionality. We believe that as the shear layer vortices traverse the cove approaching the reattachment point, they undergo a secondary instability involving spanwise oscillations. Subsequent nonlinear growth and breakdown into smaller structures would result in a significant loss of coherence. The remnants of the vortices that end up inside the recirculating zone would further experience the straining effects of the cove's spanwise flow. Under such circumstances, the leftover vortices may be expected to be too weak to exert a major influence on the boundary layer on the slat bottom surface. Clearly, a 2D flow simulation is incapable of capturing the 3D flow dynamics.

Another feature that may provide a clue for the observed differences between the measurements and computations is the location of the reattachment point. In the measured vorticity field (Fig. 9), notice that the averaged positions of the shear layer reattachment points are very close to the slat trailing edge, resulting in somewhat slimmer and elongated recirculation zones. Moreover, for all AOA, the shear layer approaches the slat surface at a shallow angle. Judging by the trajectory of the shear layer, the majority of the large-scale structures are likely to be ejected through the slat gap, and only a limited number of these structures would be entrained back into the cove region. The predicted mean reattachment locations (Figs. 9a–9c) are farther away from the slat trailing edge, resulting in shorter recirculation zones and a shear layer that reattaches the wall at a nearly right angle. Under the latter circumstances, one would expect a substantial number of the shear layer vortices to turn inward and get trapped inside the recirculating region. We believe that the absence of spanwise effects in the 2D simulations may have contributed to the differences between reattachment locations.

C. Instantaneous Flow Field

Representative plots of the measured instantaneous vorticity field at the AOA values of interest are shown in Fig. 10. The global dynamics of the cove flow field is qualitatively similar at all three AOA, except for the decreasing shear layer strength with increasing AOA. The PIV resolution is just sufficient to capture the individual vortices (red lumps) and their upward convection by the shear layer. The proximity of the first vortex to the slat cusp suggests a rapid initial amplification of unsteady disturbances and a fast shear layer roll-up. The chain of vortices, having the same sign vorticity, reaffirms the convective nature of the free shear layer instabilities (coherent structures). As alluded to earlier, the majority of the vortices, after experiencing severe distortion at the reattachment point, are ejected through the gap. Only a small number of these vortices are trapped within the recirculating flow. Two other noteworthy features of the vorticity distribution are the absence of a dominant cove center vortex and the secondary separation along the slat wall. Certainly, the notion of a center vortex is rejected by the current and the earlier measurements of Takeda et al..[15] Therefore, slat noise models based on such a vortex must be reevaluated and modified. Although the PIV results near the wall must be viewed with caution due to the reflection of laser light from the surface, no intense secondary separation from the slat surface is observed in the measured fields. Within the recirculating zone, however, weak areas of negative-sign vorticity are observed. Thus far, we have been unable to deduce a consistent pattern for the negative vorticity structures.

The instantaneous vorticity plots from the 4-degree simulation are presented in Fig. 11. The two computed snapshots, roughly corresponding to time steps 1000 (Fig. 11a) and 9700 (Fig. 11b) in the sampled record of 10,000 steps, differ significantly. The vorticity field at the earlier time displays characteristics that are more analogous to the PIV measurements. Convective amplification of disturbances into a chain of discrete vortices is observed clearly.

The reattachment point is near the trailing edge, and the shear layer approaches the solid wall at an angle that is close to the experiment. Figure 11a also shows the beginning of the phase where increasingly more vortices are being drawn into the recirculating zone. The passage of these rollers over the solid surface causes the wall boundary layer to separate and roll into vortices of opposite (negative) sign vorticity. Figure 11b shows the state of the cove flow field at the later time. Over time, interaction of the negative sign vortices with the cusp region disrupts the normal development of the shear layer, instigating a rapid roll-up of the detached shear layer into a large vortex. These larger vortices are quite disruptive in nature, distorting the path and shape of the shear layer that separates the accelerating external flow and the interior cove flow. Also note from Fig. 11b that the reattachment point has now moved farther inboard of the slat trailing edge and less vorticity is ejected through the gap. The flow fields associated with the 6- and 8-degrees AOA display similar behavior to the 4-degree case and therefore are not discussed. For completeness, a sample plot of the cove instantaneous vorticity field for 8-degree AOA is shown in Fig. 12.

In general, the comparison between computational snapshots and PIV images indicates that the simulated flow field evolves into a more energetic and chaotic pattern of vortex structures than the measurements seem to indicate. This is not entirely unexpected in view of the neglect of turbulence production (i.e., eddy diffusivity) associated with the fluctuation scales that are unresolved by the 2D, laminar cove computation. An encouraging aspect of the comparison is that the strength of the measured slat cove structures appears to be in between the predictions with a conventional URANS approach[10] and the zonal model based on a laminar cove. However, the more important and challenging question is what refinements to the zonal model would be necessary to maintain the cove flow field close to the state observed in the initial segments of the time record (Fig. 11a) rather than the more established chaotic state of the later segments (Fig. 11b). The present computations do not answer this question. However, our experience leads us to believe that refinements to the zonal model alone are less likely to produce the required fidelity in near-field simulation and that the effects of 3-D motions will also need to be accounted for in order to bridge the present gap between computations and the experiment.

D. Computed Acoustic Radiation

Microphone arrays have become a valuable tool for mapping out the characteristics of flow-induced noise sources. Nevertheless, potential effects of tunnel wall interference and interpretation of the measured noise under such circumstances remain an important issue, particularly when the tunnel walls are relatively close to the noise source. Although the primary focus of the present work was on validating the slat cove flow field (and the flow solver used was only second-order accurate), the current simulation also highlights the tunnel wall interference effects on the radiated acoustic field as described below.

Figure 13 shows an instantaneous snapshot of the computed fluctuating pressure field within the front portion of the BART test section for 4-degree AOA. The figure clearly displays propagating pressure waves emanating from the slat. Even though slat noise is composed of many frequencies, two distinct wave patterns are highlighted. The high-frequency waves, with the epicenter at the slat trailing edge, are due to vortex shedding from the finite thickness edge. The low-frequency waves, also radiating from the slat, are generated by the cove shear layer vortices via their interaction with the solid wall and ejection through the slat gap. Notice that the figure shows a reflected low-frequency wave from the tunnel floor, which is relatively close to the test model in the BART configuration. Due to reflections of this type, flow-acoustic interaction may also play a role in altering the development of the cove flow field. Certainly, using such simulations to derive useful information concerning the acoustic radiation in free flight becomes a challenging task.

VI. Concluding Remarks

A combined experimental and computational study focused on understanding the unsteady flow structures in a slat cove region was undertaken. The effort is geared towards detailed validation of the near field flow simulations. Following our previous computational framework, the turbulence production term was turned off within the cove region to suppress the extraneous diffusive effects of the turbulence model. Comparison of the simulated fields at several angles of attack with corresponding measurements shows relatively good agreement for the averaged velocity field. Greater differences are observed between the computed vorticity distributions and those inferred from the PIV data. Specifically, the predicted instantaneous vorticity field in the cove shows shear-layer vortices with more energy and a recirculating zone that is more dynamic than those indicated by the measurements. In an attempt to resolve this significant discrepancy, our future work will focus on 3D effects on the flow structures within the slat cove region and their implications for the far field noise.

Acknowledgments

The authors gratefully acknowledge valuable assistance by Dr. David Lockard of NASA Langley Research Center during the course of this investigation. Thanks are also due to Mr. M.R. Wiese of the Analytical Services and Materials, Inc. for generating the grid used during the computations.

References

1. Jenkins, L.N., Khorrami, M.R., and Choudhari, M., "Characterization of Unsteady Flow Structures Near Leading-Edge Slat: Part I. PIV Measurements," AIAA Paper 2004-2801, 2004.

2. Storms, B.L., Ross, J.C., Horne, W.C., Hayes, J.A., Dougherty, R.P., Underbrink, J.R., Scharpf, D.F., and Moriarty, P.J., "An Aeroacoustic Study of an Unswept Wing with a Three-Dimensional High Lift System," NASA TM 112222, Feb. 1998.

3. Choudhari, M., Lockard, D.P., Macaraeg, M.G., Singer, B. A., Streett, C.L., Neubert, G.R., Stoker, R.W., Underbrink, J.R., Berkman, M.E., Khorrami, M.R., and Sadowski, S.S., "Aeroacoustic Experiments in the Langley Low-Turbulence Pressure Tunnel," NASA/TM 2002-211432, Feb. 2002.

4. Storms, B.L., Hayes, J.A., Moriarty, P.J., and Ross, J.C., "Aeroacoustic Measurements of Slat Noise on a Three-Dimensional High-Lift System," AIAA Paper 99-1957, May 1999.

5. Hayes, J.A., Horne, W.C., Soderman, P.T., and Bent, P.H., "Airframe Noise Characteristics of a 4.7% Scale DC-10 Model," AIAA Paper 97-1594, May 1997.

6. Dobrzynski, W., Nagakura, K., Gehlhar, B., and Buschbaum, A., "Airframe Noise Studies on Wings with Deployed High-Lift Devices," AIAA Paper 98-2337, 1998.

7. Chow, L.C., Mau, K., and Remy, H., "Landing Gears and High Lift Devices Airframe Noise research," AIAA Paper 2002-2408, June 2002.

8. Khorrami, M.R., Berkman, M.E., and Choudhari, M., "Unsteady Flow Computations of a Slat with a Blunt Trailing Edge," AIAA J., Vol. 38, No. 11, pp. 2050-2058, Nov. 2000.

9. Singer, B.A., Lockard, D.P., and Brentner, K.S., "Computational Aeroacoustic Analysis of Slat Trailing-Edge Flow," AIAA J. Vol. 38, No. 9, pp. 1558-1564, Sept. 2000.

10. Khorrami, M.R., Singer, B.A., and Berkman, M.E., "Time-Accurate Simulations and Acoustic Analysis of Slat Free-Shear Layer," AIAA J., Vol. 40, No. 7, pp. 1284-1291, July 2002.

11. Khorrami, M.R., Singer, B.A., and Lockard, D.P., "Time-Accurate Simulations and Acoustic Analysis of Slat Free-Shear-Layer: Part II," AIAA Paper 2002-2579, June 2002.

12. Choudhari, M., Khorrami, M.R., Lockard, D.P., Atkins, H., and Lilley, G., "Slat Cove Noise Modeling: A Posteriori Analysis of Unsteady RANS Simulations," AIAA Paper 2002-2468, 2002.

13. Khorrami, M.R., Choudhari, M., Singer, B.A., Lockard, D.P., and Streett, C.L., "In Search of the Physics: The Interplay of Experiment and Computation in Slat Aeroacoustics," AIAA Paper 2003-0980, Jan. 2003.

14. Khorrami, M.R., "Understanding Slat Noise Sources," In Proceedings of EUROMECH Colloquium 449, Computational Aeroacoustics: From Acoustic Sources Modeling to Far-Field Radiated Noise Prediction, Chamonix, France, Dec. 2003.

15. Takeda, K. Ashcroft, G.B, and Zhang, X., "Unsteady Aerodynamics of Slat Cove Flow in a High-Lift Device Configuration," AIAA Paper 2001-0706, Jan. 2001.

16. Terracol, M., Labourasse, E., Manoha, E., and Sagaut, P., "Simulation of the 3D Unsteady Flow in a Slat Cove for Noise Prediction," AIAA Paper 2003-3110, May 2003.

17. Menter, F., "Improved Two-Equation k-ω Turbulence Models for Aerodynamic Flows," NASA TM 103975, 1992.

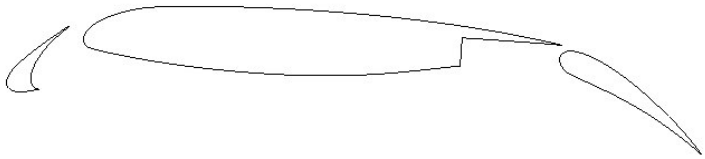

Fig. 1. Cross-sectional view of three-element 30P30N high-lift system.

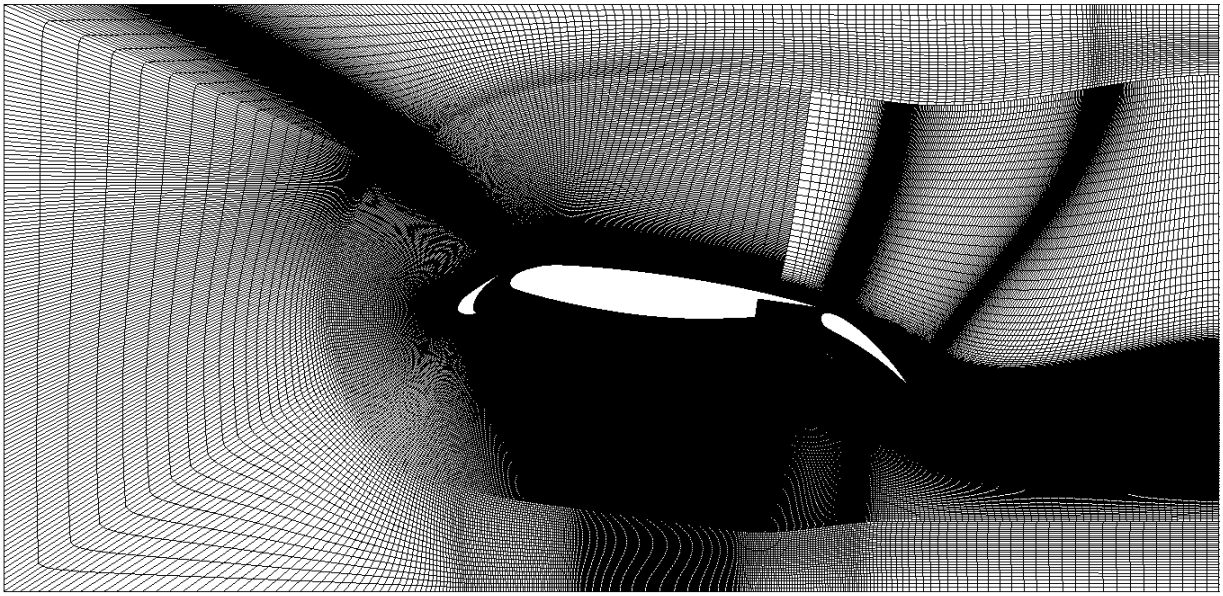

Fig. 2. Grid distribution for 30P30N model in BART.

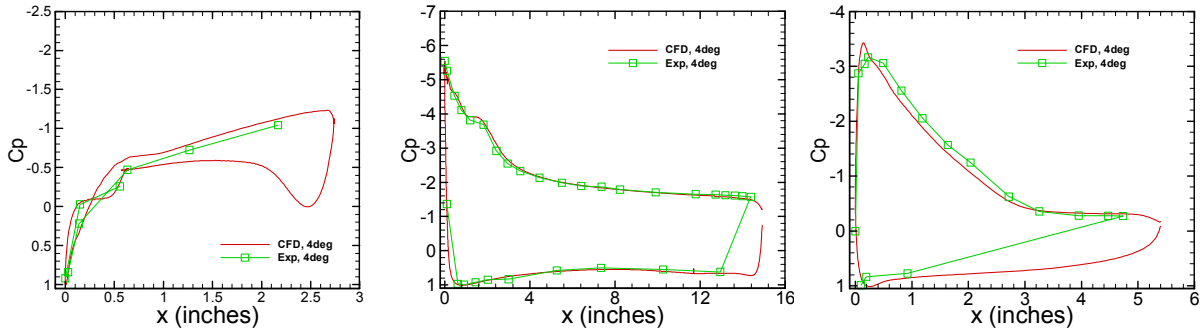

a) Slat **b) Main element** **c) Flap**

Figure 3: Surface pressure distribution for 4-degree AOA.

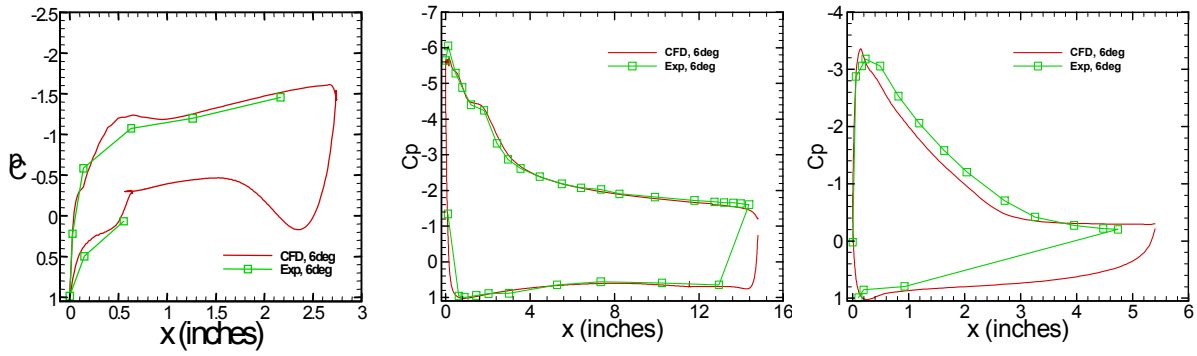

a) Slat **b) Main element** **c) Flap**

Figure 4: Surface pressure distribution for 6-degree AOA.

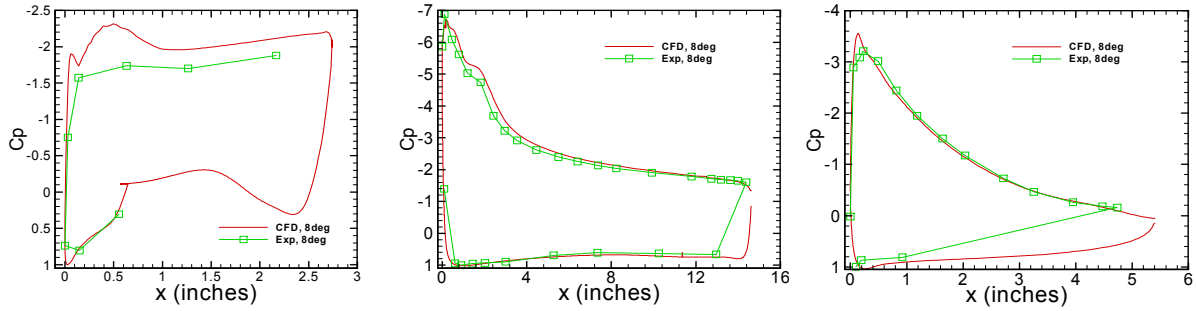

a) Slat **b) Main element** **c) Flap**

Figure 5: Surface pressure distribution for 8-degree AOA.

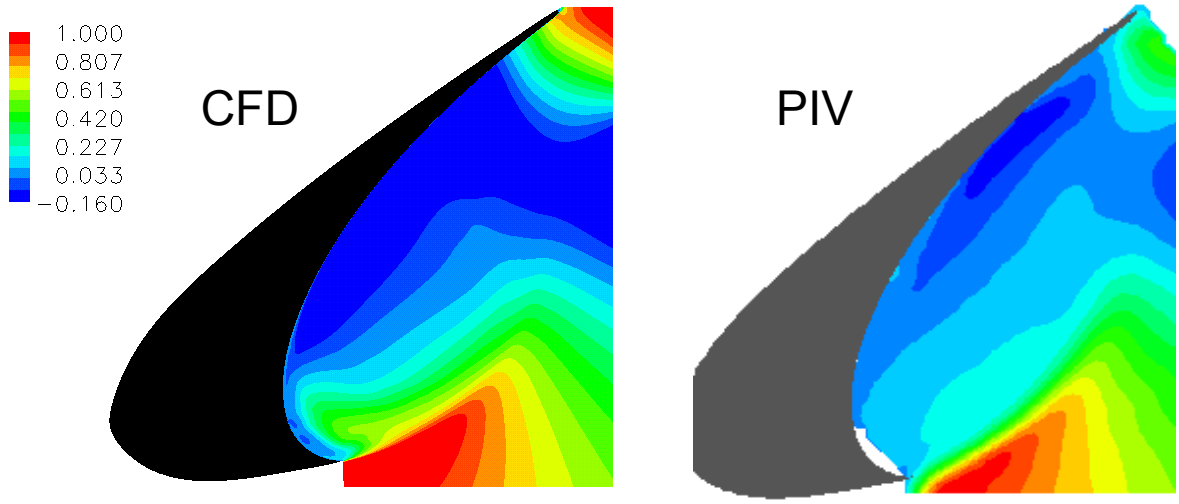

a) Streamwise velocity

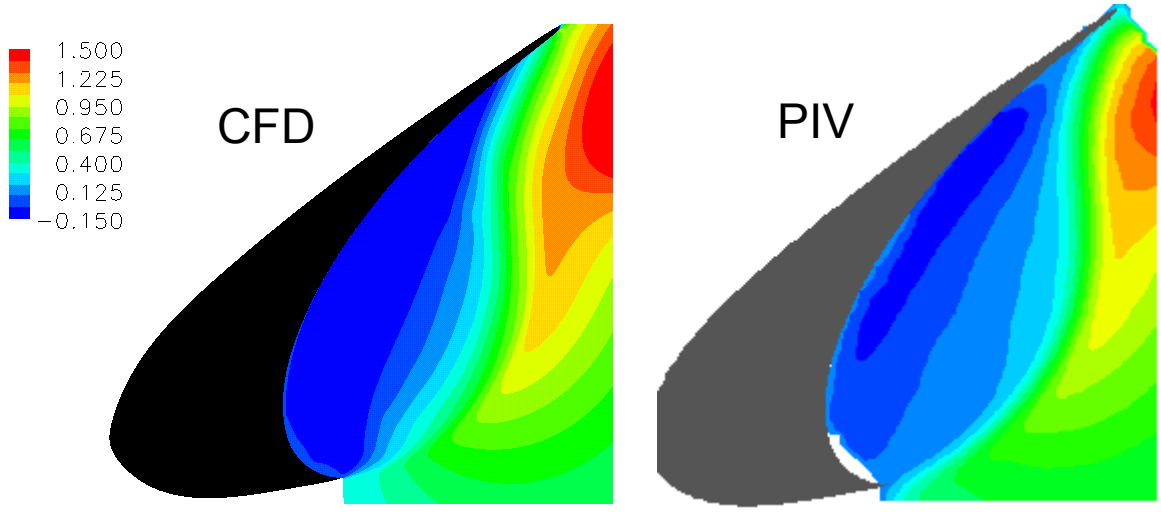

b) Vertical velocity

Figure 6: Averaged velocity field for 4-degree AOA.

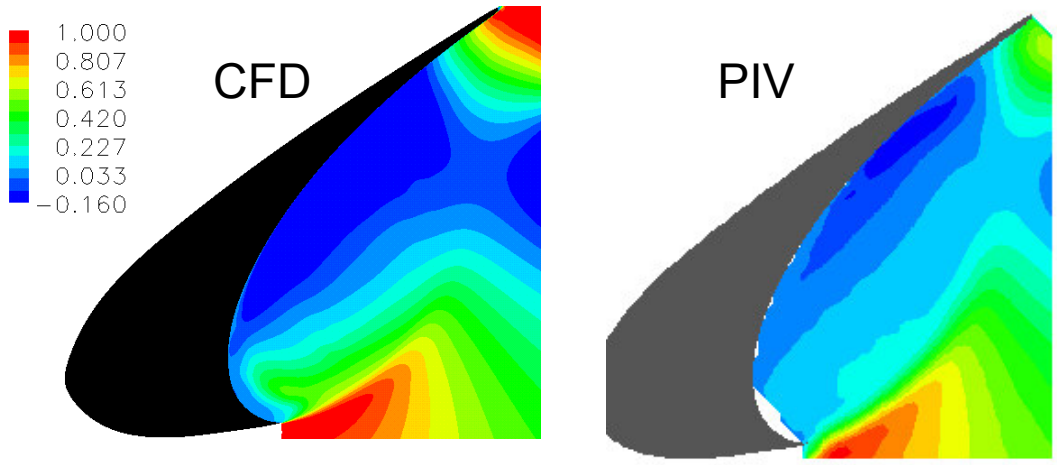

a) Streamwise velocity

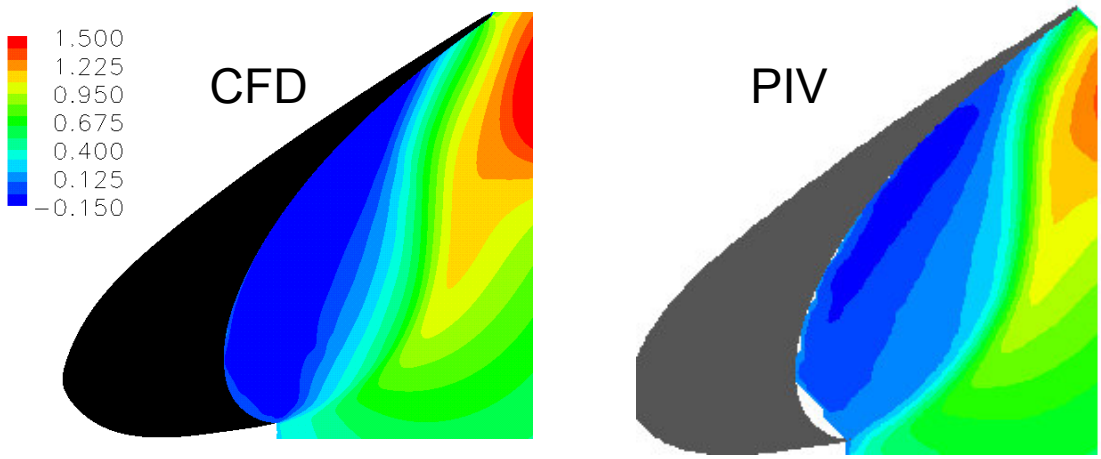

b) Vertical velocity

Figure 7: Averaged velocity field for 6-degree AOA.

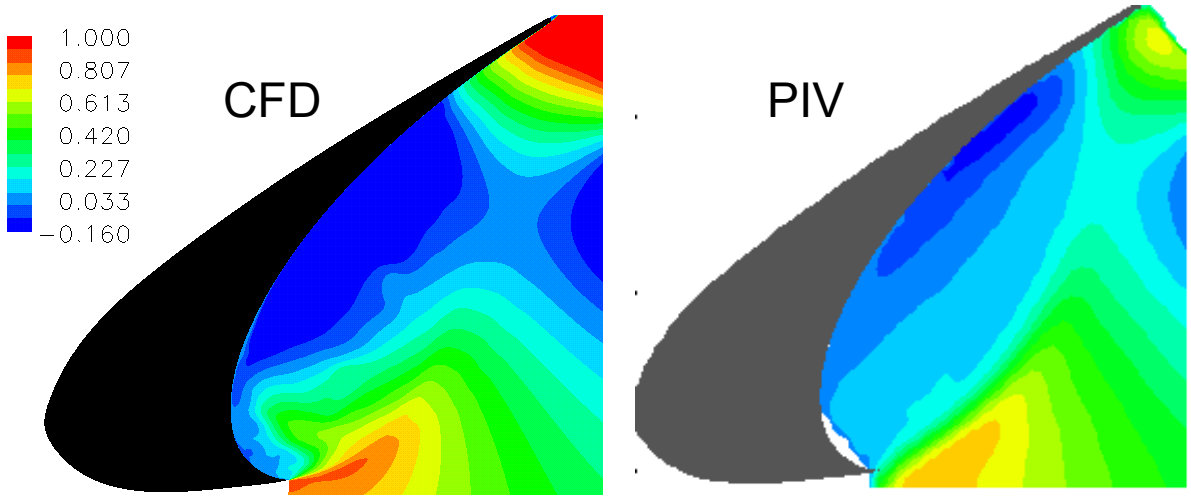

a) Streamwise velocity

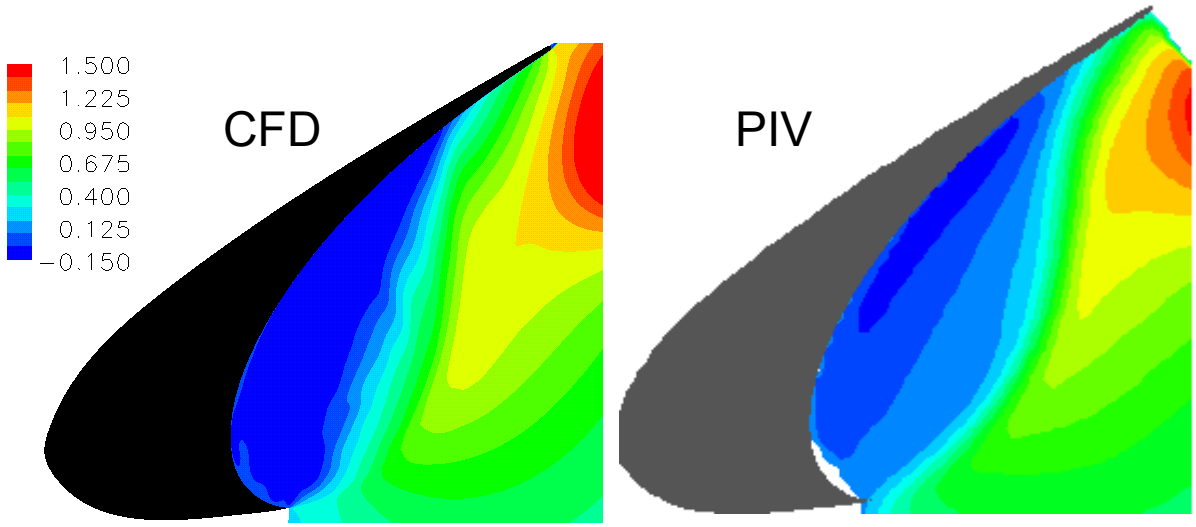

b) Vertical velocity

Figure 8: Averaged velocity field for 8-degree AOA.

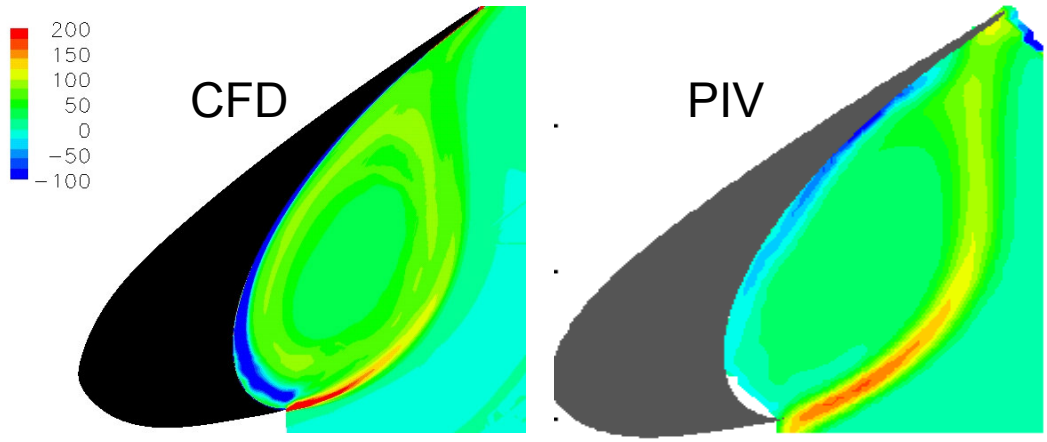

a) 4-degree AOA

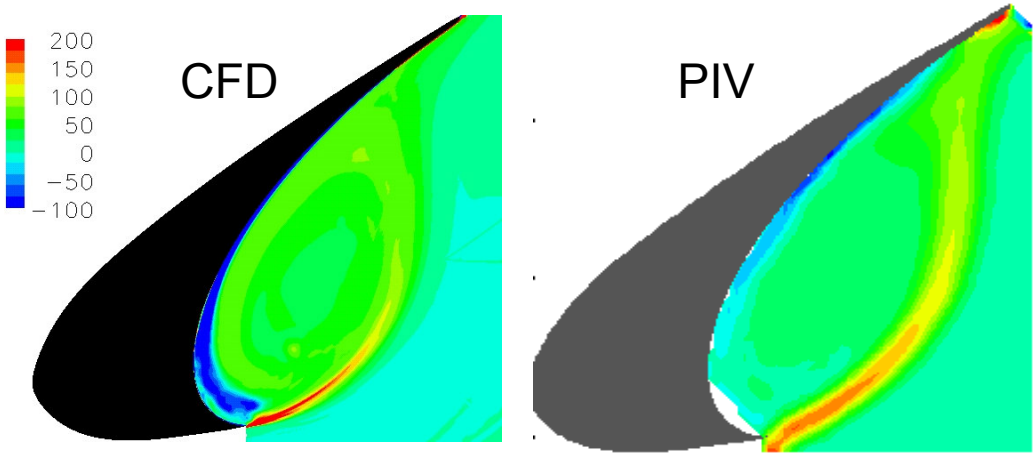

b) 6-degree AOA

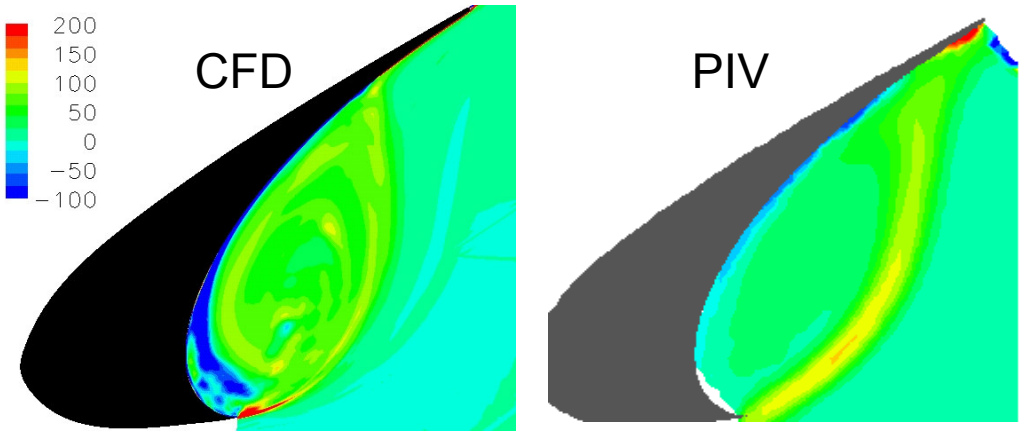

c) 8-degree AOA

Figure 9: Averaged vorticity field.

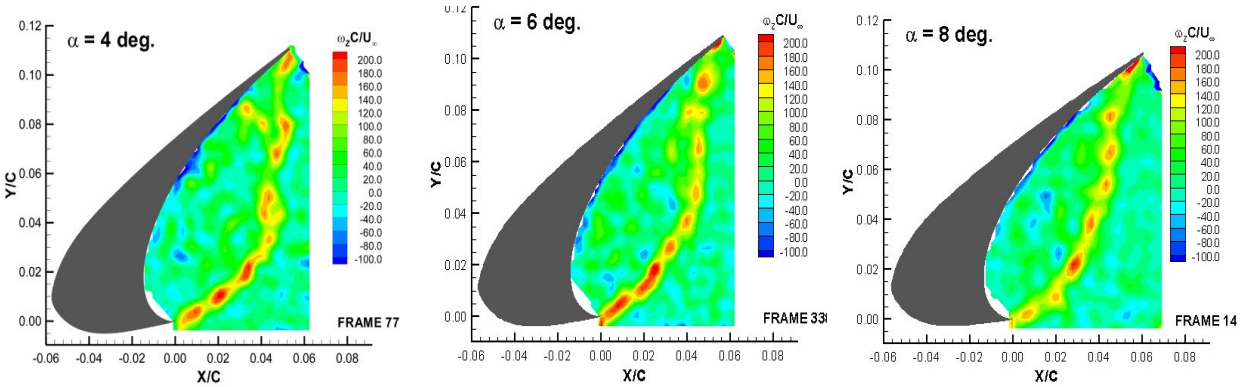

Figure 10: Sample instantaneous vorticity field from PIV measurements.

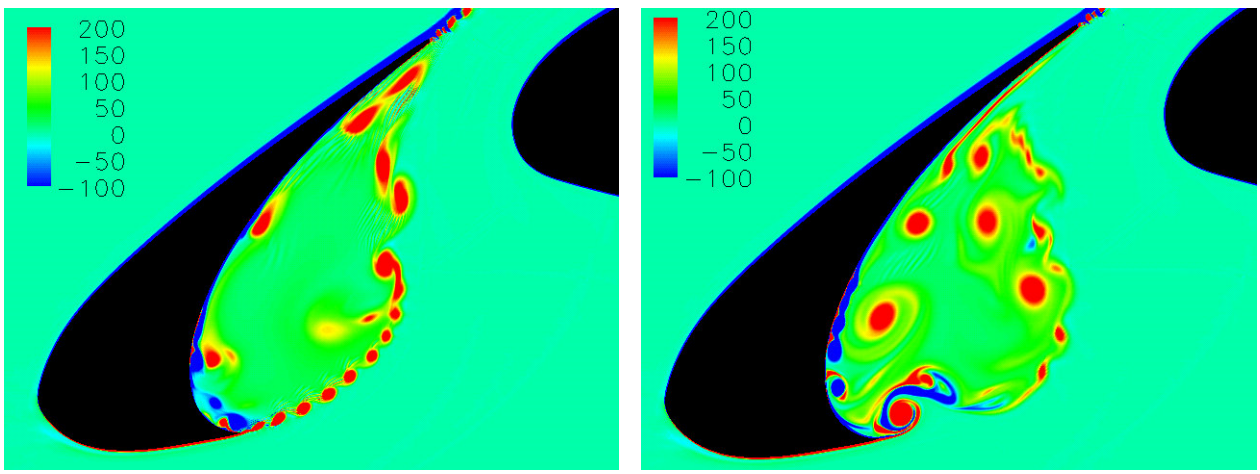

a) Towards the beginning of simulated time record **b) Towards the end of simulated time record**

Figure 11: Computed instantaneous vorticity field for 4-degree AOA.

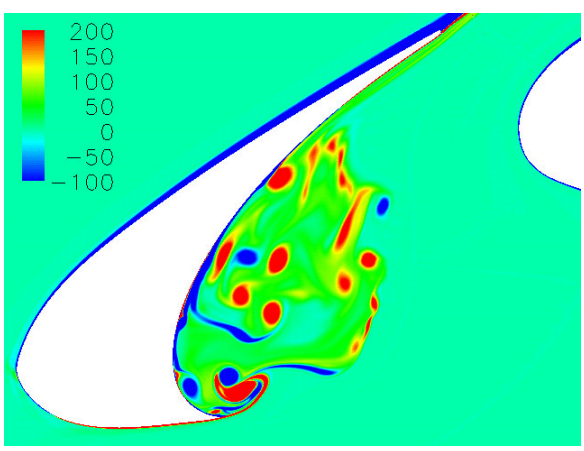

Figure 12: Computed instantaneous vorticity field for 8-degree AOA.

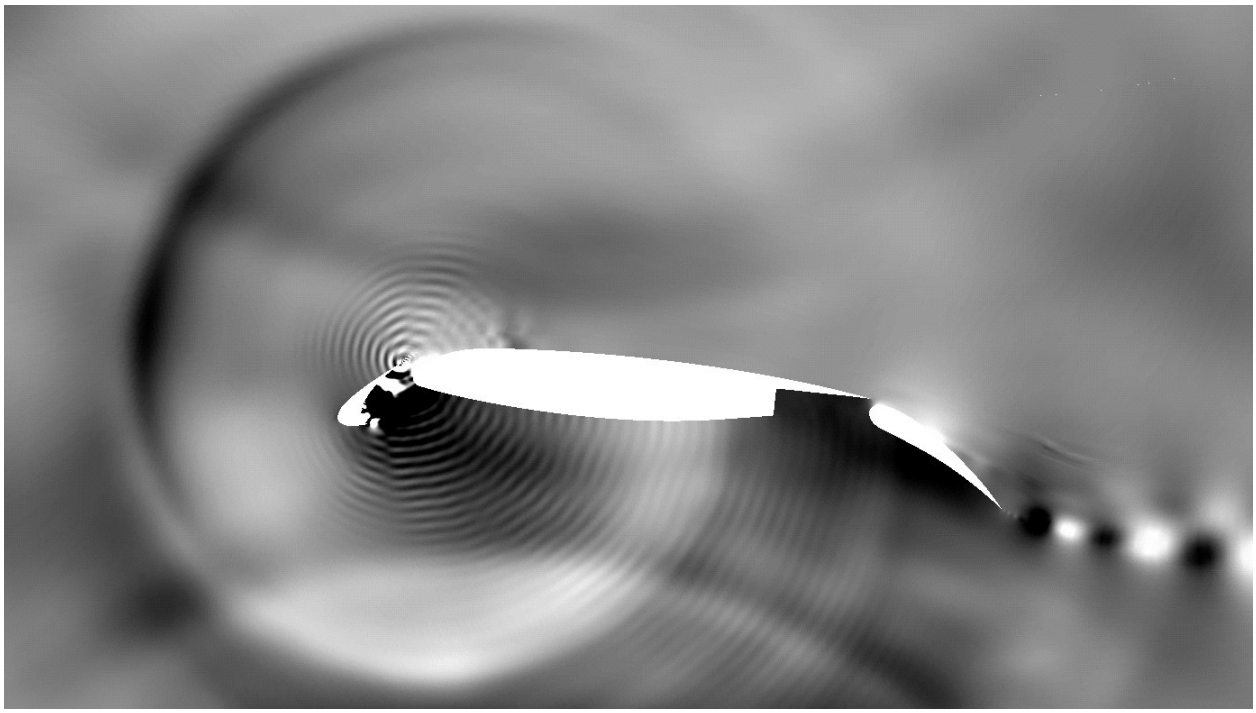

Figure 13: Instantaneous pressure fluctuation field at 4-degree AOA.